Energy Conversion and Management 341 (2025) 120062

Contents lists available at ScienceDirect

Energy Conversion and Management

journal homepage: www.elsevier.com/locate/enconman

Theoretical limitation for achieving chemical and thermal energy via synergizing solar non-thermal and thermal effects in the concentrating system

Yuan Gao, Chenyu Xu, Entao Zhang, Xuan Zhu, Yin Xie, Yanwei Zhang *

State Key Laboratory of Clean Energy Utilization, Zhejiang University, Hangzhou 310027, China

A B S T R A C T

Photothermal chemistry (PTC) systems offer a promising route for efficiently converting solar energy into both chemical and thermal energy. However, the theoretical understanding of how high-temperature thermal effects in PTC systems influence non-thermal effects and chemical exergy efficiency (η_{chem}) remains limited. In this study, we establish a theoretical framework for high-temperature PTC systems by coupling carrier balance (CB) with lattice thermal equilibrium (TE), and apply it to an idealized PTC system. Our analysis demonstrates that the complex impact of thermal effects on non-thermal effects—including semiconductor photoelectric performance and chemical reaction thermodynamics—can be effectively characterized by a single parameter: the quantum efficiency of the current ($\eta_{quantum}$). By modulating the semiconductor temperature to enhance $\eta_{quantum}$, thermal and non-thermal effects can be synergistically coordinated, enabling η_{chem} to exceed 32 %. Furthermore, we propose a generalized strategy for manipulating thermal effects to jointly optimize η_{chem} and thermal exergy efficiency ($\eta_{thermal}$), thereby maximizing the total exergy efficiency (η_{total}) of PTC systems. Broad-range calculations demonstrate that the theoretical η_{total} of high-temperature PTC systems can exceed 37 % under standard mode and surpass 60% under full-spectrum mode. This work provides a robust framework for understanding and optimizing high-temperature PTC systems, contributing to unlocking their potential as highly efficient and sustainable energy solutions.

1. Introduction

Solar energy, characterized by its abundance and renewability, represents a cornerstone for achieving carbon neutrality [1,2]. Converting solar energy with semiconductors is an effective harnessing method [3–5]. In this process, solar radiation excites carriers of semiconductors to produce electrical energy (as in photovoltaics) [6–8] or to drive chemical reactions (as in photochemistry systems) [9–11], thereby exhibiting non-thermal effects. Solar thermal effects are also inevitably generated due to electron–phonon interactions within semiconductors, such as the thermalization of photoexcited carriers and isothermal dissipation [12].

Using concentrated radiation is an usual method to enhance energy conversion efficiency in photovoltaics and photochemistry systems, and the corresponding systems are concentrated photovoltaics (CPV) [13,14] and photothermal chemistry (PTC) systems [15], respectively. In CPV and PTC systems, thermal effects become more significant due to the increasing temperatures [16–18], which effectively increases the thermal exergy efficiency ($\eta_{thermal}$) of systems but also significantly influences non-thermal effects. In CPV systems, the thermal effect exacerbates carrier recombination, which degrades the photoelectric performance of semiconductors [19]. Therefore, high-temperature thermal effects are usually removed by enhancing heat transfer [20,21], preventing the degradation of photoelectric performance and simultaneously boosting thermal exergy output [22,23], eventually improving total exergy efficiency (η_{total}) of systems. In PTC systems, however, the influence of thermal effects on non-thermal effects is more complex. While suppressing thermal effects may benefit the photoelectric performance of semiconductors, it could simultaneously diminish their facilitating effects in promoting the thermodynamics and kinetics of chemical reactions [24–26]. In fact, advanced PTC systems have leveraged their facilitating effects to achieve chemical exergy efficiencies (η_{chem}) exceeding 20 % [27,28]. Therefore, optimizing η_{total} in PTC systems requires a clear elucidation of the complex interplay between thermal and non-thermal effects at the theoretical level.

In high-temperature PTC systems, lattice vibrations in semiconductors become increasingly pronounced and exhibit significant interaction with carrier balance (CB) [35]. Therefore, it is essential to establish lattice thermal equilibrium (TE) and to couple TE with CB in the theoretical model. Prior studies in CPV systems have demonstrated that CB–TE coupling primarily involves two key relationships [36,37]: (1) thermal source terms in TE arise from specific physical processes in CB, where electron–phonon interactions generate thermal energy [38];

* Corresponding author.
E-mail address: zhangyw@zju.edu.cn (Y. Zhang).

https://doi.org/10.1016/j.enconman.2025.120062
Received 18 February 2025; Received in revised form 15 May 2025; Accepted 9 June 2025
Available online 17 June 2025

Nomenclature

E_{ele}	power of extracted carriers
E_{g0}	bandgap of semiconductor catalyst
E_g	bandgap of semiconductor catalyst at 298.15 K
E_{in}	power of AM 1.5G spectrum
E_{iso}	power of isothermal dissipation
E_{nonrad}	power of non-radiative recombination
E_{rad}	power of radiative recombination
E_S	power of excited carriers
E_{the}	power of thermalization
F_{nonrad}	non-radiative recombination rate of carriers
F_{rad}	radiative recombination rate of carriers
F_s	excitation rate of carriers
I	current of the PTC system
n	photon number of unit energy (AM1.5G spectrum)
N_A	Avogadro's constant
q	elementary charge
Q_{con}	convective heat transfer power
$Q_{conduction}$	conductive heat transfer power
Q_{rad}	radiative heat transfer power
Q_{rec}	reaction heat power
Q_{source}	thermal source power
T_0	ambient temperature, 298.15 K
T_{gap}	difference between T_{sem} and T_{outlet}
T_{outlet}	the outlet temperature of HTF
T_{sem}	temperature of semiconductor catalysts
V_{chem}	operating voltage
$\Delta_r G$	Gibbs free energy change of chemical reactions
η_{chem}	chemical exergy efficiency
η_{Eele}	ratio of E_{ele} to incident solar power
$\eta_{quantum}$	ratio of carrier extraction rate to photon incidence rate
$\eta_{thermal}$	thermal exergy efficiency
η_{total}	total exergy efficiency

Abbreviations

C	concentration ratio
CB	carrier balance
CPV	concentrated photovoltaic
EMF	electromotive force of chemical reactions
H	height of the microchannel
HTF	heat transfer fluid
PTC	photothermal chemistry
TE	lattice thermal equilibrium

and (2) the semiconductor temperature (T_{sem}) in CB is determined by TE [39]. However, these findings have not yet been applied to PTC systems. Most existing theoretical models of PTC systems focus solely on establishing CB to describe carrier dynamics, while TE and CB–TE coupling are generally not implemented (Table 1) [40]. The absence of CB–TE coupling affects the accuracy of both thermal and non-thermal effect predictions. Specifically, without CB–TE coupling, TE cannot receive thermal source terms from CB, and the temperatures used in both CB and TE must be artificially prescribed. For most low-temperature PTC models, thermal effects are relatively minor, and prescribing the temperature as T_0 introduces negligible error [30,31]. In high-temperature PTC systems, however, manually assigning the temperature introduces substantial errors [34]. The errors not only prevent the accurate determination of $\eta_{thermal}$ and η_{total}, but also propagate errors into non-thermal effects via the temperature-dependent terms in CB, ultimately compromising the accuracy of the chemical exergy efficiency (η_{chem}). In fact, the temperature in high-temperature PTC systems can—and should—be computed self-consistently through CB–TE coupling when parameters such as C, E_g, and heat transfer conditions are specified. Although manually prescribing the temperature allows exploration of arbitrary temperature ranges, it is physically inconsistent.

In this work, a theoretical model for high-temperature PTC systems is developed by establishing CB-TE coupling, and is applied to an idealized PTC system. The results reveal that the combined influence of thermal effects on non-thermal processes—including chemical reactions and semiconductor performance—can be effectively characterized by a single parameter: the quantum efficiency of the current ($\eta_{quantum}$). By modulating the semiconductor temperature to enhance $\eta_{quantum}$, thermal and non-thermal effects can be synergistically coordinated, enabling η_{chem} to exceed 32 %. Furthermore, we propose a generalized strategy for manipulating thermal effects to jointly optimize η_{chem} and $\eta_{thermal}$, thereby maximizing η_{total} of PTC systems. Extensive calculations prove that the theoretical η_{total} can exceed 37 % under standard mode and surpass 60 % under full-spectrum utilization. This work emphasizes the vast potential of high-temperature PTC systems for efficiently converting solar energy into exergy, laying a robust foundation for advancing the understanding and optimization of these systems.

Table 1
Existing theoretical models of PTC systems.

Number	Temperatur[e] (K)	CB[d]	TE[d]	CB-TE coupling[d]	η_{chem} [e] (%)	$\eta_{thermal}$ [e] (%)	η_{total} [e] (%)	Ref.
1	300	Y	–	–	30.7	N/A	N/A	[29]
2	300	Y	–	–	~26	N/A	N/A	[30]
3	300	Y	–	–	31.1	N/A	N/A	[31]
4	300–353	Y	–	–	30.8	N/A	N/A	[32]
5	300–350	Y	–	–	29.8	N/A	N/A	[33]
6	300–310	Y	–	–	~30	N/A	N/A	[28]
7	400–900	Y	Y	–	~16	N/A	N/A	[34]
8[a]	344	Y	Y	Y	32.1	2.5	34.6	This work
9[b]	538	Y	Y	Y	29.7	7.9	37.6	This work
10[c]	669	Y	Y	Y	16.5	46.4	62.9	This work

[a] Maximum η_{chem} in standard PTC system.
[b] Maximum η_{total} in standard PTC system.
[c] Maximum η_{total} in full-spectrum PTC system.
[d] Y and – represent the presence or absence, respectively.
[e] N/A indicates that the exergy efficiency cannot be calculated due to the absence of CB–TE coupling.

2. Modeling methodology

2.1. Ideal PTC system

The decomposition of CO_2 was selected as the target reaction, which is widely studied in the field of photothermal chemistry [41]. As a pure gaseous reaction, it avoids complications related to phase change:

$$CO_2 = CO + \frac{1}{2}O_2 \tag{1}$$

An ideal PTC system is designed in this study (Fig. 1a). To enhance heat transfer effectively, a dual-channel configuration is employed. In the Channel 1, CO_2 flows as the reactant gas at a rate of 0.06 kg/s. CO_2 cannot function as the HTF in Channel 2 due to its poor heat transfer performance and low density [42]. Therefore, high-temperature thermal oil is used as the HTF to cool the semiconductor catalyst [43]. Channel 1 outputs a high-temperature gas mixture consisting of the generated CO and O_2, along with unreacted CO_2. Channel 2 delivers high-temperature HTF. The gas mixture and HTF are separately introduced into an ideal Carnot heat engine, where they are cooled down to the T_0 while producing exergy. The resulting $\eta_{thermal}$ is given by:

$$\eta_{thermal} = \frac{Q_{con} \times \left[1 - \left(\frac{T_0}{T_{outlet}}\right)\right]}{CE_{in}} \tag{2}$$

Q_{con} refers to the convective heat transfer power between the PTC system and both HTF and gas mixture. T_{outlet} is the outlet temperature of the HTF. E_{in} represents the power of the AM 1.5G spectrum.

After passing through the Carnot heat engine, the gas mixture at T_0 is fed into an isothermal and isobaric reversible fuel cell, where the reverse reaction of Equation (1) takes place. The released Gibbs free energy is fully converted into exergy. The resulting η_{chem} is given by:

$$\eta_{chem} = \frac{E_{chem}}{CE_{in}} = \frac{I\Delta_r G(T_0)}{2qN_A CE_{in}} \tag{3}$$

I Is the current of the PTC system. $\Delta_r G(T_0)$ represents the Gibbs free energy released by the reverse reaction at T_0. N_A represents Avogadro's constant. The factor of 2 corresponds to the number of electrons transferred during the reaction. The pure CO_2 produced at the outlet of the fuel cell, along with the cooled HTF, are fed into the two channels of the PTC system to initiate a new cycle

The η_{total} of the system are defined as

$$\eta_{total} = \eta_{chem} + \eta_{thermal} \tag{4}$$

The idealized system is established based on the following assumptions:

(1) The catalysts are treated as ideal semiconductors, exhibiting no non-radiative recombination, and the radiative recombination coefficient is temperature-independent.
(2) The catalyst plate is sufficiently thin to ensure thermal uniformity across its upper and lower surfaces.
(3) The lower surface of the catalyst plate is surface-treated to exhibit near-zero emissivity in the long-wavelength range, effectively eliminating radiative heat loss.
(4) The effects of mass transport and chemical reaction kinetics are neglected; as a result, CO_2 decomposition is assumed to occur T_{sem}.
(5) Due to the low mass flow rate of CO_2, the outlet gas mixture is presumed to equilibrate at T_{sem}.
(6) Both the reactor enclosure and the cover plate are considered perfectly transparent and adiabatic.

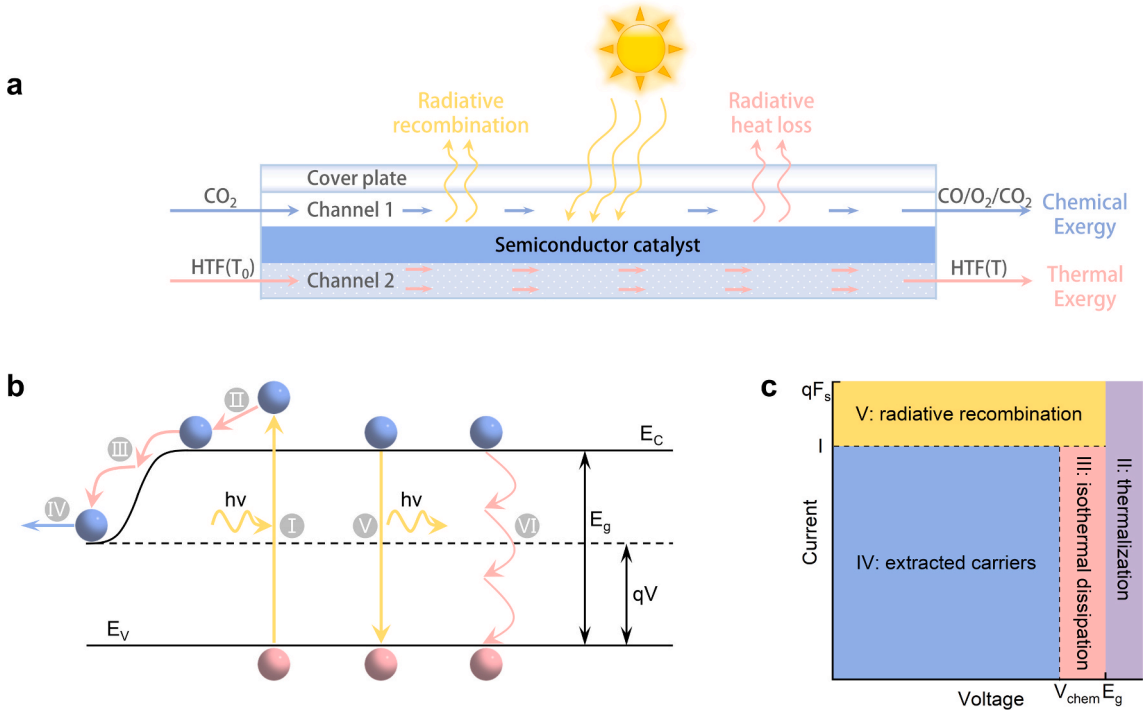

Fig. 1. Schematic of the ideal PTC system and CB in semiconductor catalysts. (a) The schematic of the ideal PTC system. (b) Carrier dynamics within the semiconductor, including I) carrier excitation, II) thermalization, III) isothermal dissipation, IV) extraction and utilization in the chemical reaction, V) radiative recombination: an electron in the conduction band recombines with a hole in the valence band and the excess energy is emitted in the form of a photon. VI) non-radiative recombination: electrons and holes recombine and release phonons instead of photons. The yellow and pink arrows represent the absorption (emission) of photons and phonons, respectively. The phonons are not explicitly depicted. (c) Energy diagram of Processes II-V in (b). Process VI is not depicted, as non-radiative recombination is zero in an ideal semiconductor. The sum of energy from Process II to V is the total energy of excited carriers in Process I. F_s, I, E_g and V_{chem} are the rates of carrier generation, current, bandgap, and operating voltage, respectively.

(7) In the full-spectrum mode, a heat-collecting membrane is integrated beneath the catalyst plate, fully converting the portion of light that is not absorbed by the catalyst plate into thermal energy. The membrane has the same temperature as the catalyst plate due to its thin structure and close contact with the catalyst plate.

2.2. CB

The CB with temperature effects is expressed as: [40]

$$F_s(T) - F_{rad}(V,T) - F_{nonrad}(V,T) - \frac{I(V,T)}{q} = 0 \tag{5}$$

Here, F_s, F_{rad}, F_{nonrad}, are the rates of carrier excitation, radiative recombination, and nonradiative recombination, respectively. q denotes the elementary charge. The calculation methods for F_s, F_{rad} are detailed in Supplementary Note 1.F_{nonrad} is zero for the ideal semiconductor. Unless otherwise specified, V and T in this study refer to the operating voltage (V_{chem}) and the temperature of semiconductor catalysts (T_{sem}), respectively. All terms in CB are functions of V_{chem}, T_{sem} and the bandgap [19], with the bandgap also being a function of T_{sem} (Supplementary Note 2, Fig. S1) [44,45]. V_{chem} equals to the electromotive force of the chemical reaction (EMF), which depends on the reaction temperature (Supplementary Note 3). Since the effects of mass transfer and chemical reaction kinetics are neglected, CO_2 decomposition is assumed to occur at the semiconductor temperature (T_{sem}). Thus:

$$V_{chem} = EMF(T_{sem}) \tag{6}$$

2.3. TE and CB-TE coupling

The TE in the semiconductor is given expressed as: [42]

$$Q_{source}(T) = Q_{conduction}(T) + Q_{con}(T) + Q_{rad}(T) + Q_{rec}(T) \tag{7}$$

$Q_{source}(T)$ is the thermal source term. Thermal output terms include $Q_{conduction}$, Q_{con} and Q_{rad}, which correspond to the power of conduction, convection, and radiation heat transfer, respectively. Q_{rec} represents the reaction heat power (Supplementary Note 3).

The coupling between CB and TE can be summarized into two relationships. The first coupling relationship is that $Q_{source}(T)$ in TE originate from CB. Therefore, the energy conservation based on CB should be established first:

$$E_S(T) = E_{the}(V,T) + E_{iso}(V,T) + E_{ele}(V,T) + E_{rad}(V,T) + E_{nonrad}(V,T) \tag{8}$$

Here, E_S, E_{the}, E_{iso}, E_{ele}, E_{rad}, E_{nonrad} are powers of excited carriers, thermalization, isothermal dissipation, extracted carriers, radiative recombination, and non-radiative recombination, respectively [46]. Isothermal dissipation represents the energy dissipated as heat due to the difference between E_g and qV_{chem} [12]. The diagrams of each term are shown in Fig. 1b-c, with detailed formulas provided in Supplementary Note 4.

It can be seen that three processes in CB generate thermal energy via electron–phonon interactions, including thermalization, isothermal dissipation, and non-radiative recombination. Therefore, TE with the expanded form of $Q_{source}(T)$ is:

$$E_{the}(V,T) + E_{nonrad}(V,T) + E_{iso}(V,T) = Q_{conduction}(T) + Q_{con}(T) + Q_{rad}(T) + Q_{rec}(T) \tag{9}$$

Based on the assumptions of the ideal PTC system, $Q_{conduction}$ can be neglected. Q_{con} and Q_{rad} are determined as functions of T_{sem} through heat transfer analysis (Supplementary Note 5) [39,47].

The second coupling relationship is that T_{sem} in CB should be determined by TE. Therefore, Equations (8) and (9) together constitute the set of governing equations for CB, TE and CB-TE coupling. A computational framework for solving the set of governing equations is established (Fig. S2), which is executed using MATLAB. For comparison, a model of CPV is also developed, with its computational framework detailed in Fig. S3.

3. Influences of thermal effects on η_{chem}

3.1. V_{chem}, I and $\eta_{quantum}$

The performance of the ideal PTC system is calculated with C ranging from 100 to 1000. The E_{g0}, H and the flow rate of the ideal PTC system are set to 1.8 eV, 500 μm, and 1 kg/s, respectively. The $\eta_{quantum}$ is defined as the ratio of carrier extraction rate to photon incidence rate:

$$\eta_{quantum} = \frac{I(V,T)}{qnCE_{in}} \tag{10}$$

n represents the number of photons per unit of energy for the AM1.5G solar spectrum. $\eta_{quantum}$ consistently increases with higher C (Fig. 2a). As shown in Equation (10), an increase in $\eta_{quantum}$ requires I to grow at a rate faster than that of C, which is confirmed by comparing the current curve with the black dashed line in Fig. 2b. This faster increase in I can be attributed to two factors. First, convection cooling by the HTF effectively suppresses the rapid rise in T_{sem} as C increases. At C = 1000, T_{sem} reaches 516.7 K (Fig. 2c), which is insufficient to induce radiative recombination that could significantly degrade I (see E_{rad} in Fig. 2d). This ensures that the growth rate of I closely matches that of C. On this basis, the increase in T_{sem} leads to a reduction in the bandgap E_g, which enhances light absorption and makes the increasing rate of I beyond that of C (Fig. S4). V_{chem} decreases with increasing C due to the reduction in EMF at higher T_{sem} (Equation (6), Fig. 2b), and the temperature coefficient is relatively small ($\sim 4.5 \times 10^{-4}$ V/K, Fig. S5).

3.2. Photoelectric performance of semiconductor catalysts

The photoelectric performance of semiconductor catalysts is characterized by η_{Eele}:

$$\eta_{Eele} = \frac{V_{chem}I}{CE_{in}} \tag{11}$$

It represents the ratio of the power of extracted carriers to (E_{ele}) to incident solar power. Benefiting from effective cooling measures, η_{Eele} increases with higher C until C = 820 (Fig. 2a), which means the positive effect of increasing T_{sem} to I is larger than its negative effects on V_{chem}. However, after C > 820, the gradual decline in η_{Eele} indicates that elevated T_{sem} begins to degrade the photoelectric performance of the semiconductor.

3.3. η_{chem}

η_{chem} is jointly determined by semiconductor photoelectric performance and chemical reaction thermodynamics. When C > 820, semiconductor photoelectric performance begins to deteriorate due to thermal effects; however, η_{chem} continues to increase (Fig. 2a), which is attributed to favorable shifts in reaction thermodynamics driven by thermal effects. Interestingly, this dual influence of thermal effects can be fully captured by $\eta_{quantum}$ (Fig. 2a), which exhibits an identical trend to η_{chem}, despite variations in absolute values (Supplementary Note 7). This is because $\eta_{quantum}$ represents the number of extracted carriers, which determine the quantity of products. The Gibbs free energy released by a fixed quantity of products ($\Delta_r G(T_0)$) during the utilization process at T_0 is constant (IV process in Fig. 3a), so η_{chem} depends solely on $\eta_{quantum}$. The role of thermal effects is manifested in providing sufficient reaction heat ($Q_{rec}(T)$), bridging the gap between $\Delta_r G(T)$ in the

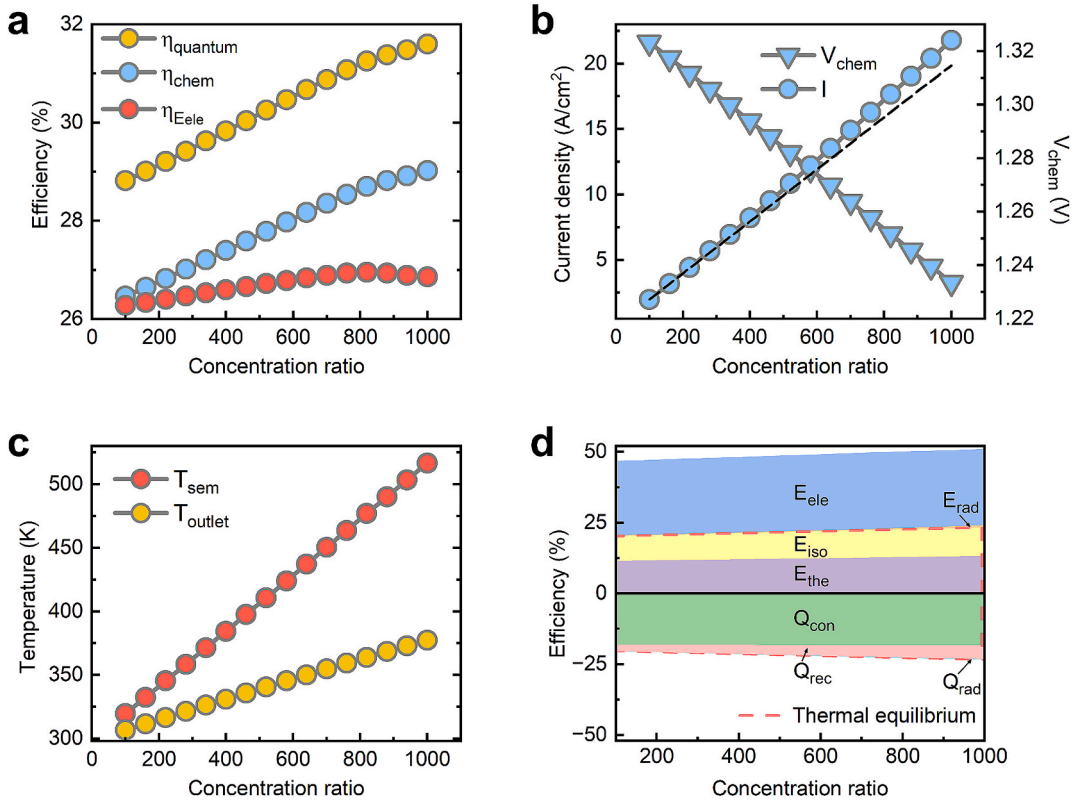

Fig. 2. Performance of the high-C PTC system. (a) Changes in $\eta_{quantum}$, η_{chem} and η_{Eele} with C. (b) Variations in V_{chem} and I with C. The black dashed line represents the current when $\eta_{quantum}$ remains constant as C increases, where the increase rate of I equals that of C. (c) Variations in T_{sem} and T_{outlet} with C. (d) Variations in energy conservation and TE of the PTC system with C. Energy efficiency is defined as $\eta_x = \frac{E_x}{CE_{in}}$, where x denotes a specific term in CB or TE. The region where $y > 0$ represents energy conservation in the PTC system, as it encompasses all output terms within the CB. The sum of these terms corresponds to the energy efficiency of the absorbed photons at a given C. The area enclosed by the pink dashed lines indicates the TE of the PTC system, with regions where $y > 0$ and $y < 0$ corresponding to the energy efficiencies of thermal source terms and thermal output terms, respectively. E_{rad} remains negligible throughout the range of C = 100 to 1000. In (a)-(d), a data point is recorded for every increment of 20 in C.

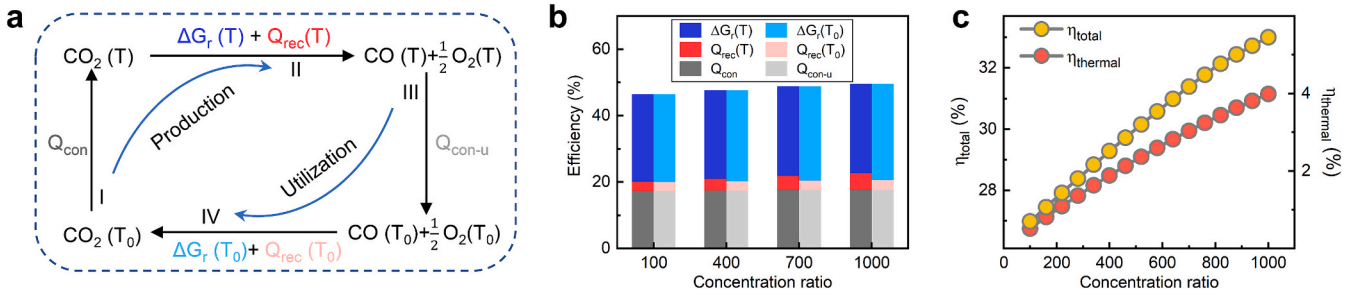

Fig. 3. Synergistic effects of semiconductor performances and chemical reactions. (a) The cycle of production and utilization in the ideal high-temperature PTC systems. I) CO_2 is heated to T and reaches the semiconductor surface. II) CO decomposes at T, absorbing the Gibbs free energy $\Delta_r G(T)$ provided by extracted carriers and thermal energy $Q_{rec}(T)$ from the reaction environment. III) The outlet CO and O_2 release thermal exergy through a Carnot heat engine, with the temperature reduced to T_0. IV) At T_0, CO and O_2 react and release chemical exergy $\Delta_r G(T_0)$ and thermal energy $Q_{rec}(T_0)$. $Q_{rec}(T_0)$ cannot be converted into exergy due to zero efficiency in the Carnot cycle. The generated CO_2 in IV initiates a new cycle. It should be noted that Q_{con} in I and Q_{con-u} in III are not strictly identical; however, the difference between them is negligible is our model (Supplementary Note 6). (b) Efficiencies of various energy terms in (a) under different C. (c) Variations in $\eta_{thermal}$ and η_{total} with respect to C.

production process (II process in Fig. 3a) and $\Delta_r G(T_0)$ in the utilization process. As shown in Fig. 3b, the increase of C leads to a rise in T_{sem}, which enlarges the difference $\Delta_r G(T_0) - \Delta_r G(T)$. However, the higher T_{sem} enhances the available reaction heat, such that the increase in $Q_{rec}(T) - Q_{rec}(T_0)$ compensates for $\Delta_r G(T_0) - \Delta_r G(T)$. This thermal contribution ensures that the cycle between production and utilization remains energetically closed and operable. By contrast, the electricity efficiency of CPV systems follows the same trend as η_{Eele}, as they lack this thermal compensation mechanism of thermal effects (Fig. S6).

4. Regulating thermal effects to optimize η_{total}

Besides enhancing η_{chem}, increasing T_{sem} at higher C results in higher $\eta_{thermal}$, collectively contributing alongside η_{chem} to the growth of η_{total} (Fig. 3c). These findings highlight the critical role of thermal effect regulation in enhancing η_{total}, underscoring the need to explore generalized strategies for modulating thermal effects. Here, two characteristic temperatures—T_{sem} and T_{gap}—are selected as key indicators for tuning thermal effects. T_{sem} influences η_{chem} by modulating the $\eta_{quantum}$, while

also directly affecting $\eta_{thermal}$. In addition, $\eta_{thermal}$ is also related to T_{gap}, which is the temperature difference between T_{sem} and the temperature of outlet HTF (T_{outlet}). A smaller T_{gap} indicates a more complete utilization of T_{sem}'s potential to produce thermal exergy.

4.1. Regulating T_{sem} by reducing the flow rate

Since the increase of T_{sem} benefits both η_{chem} and $\eta_{thermal}$ (Figs. 2a and 3c), we try to further elevate T_{sem} by reducing the flow rate of HTF. With the flow rate decreases from 1 kg/s to 0.7 kg/s, T_{sem} increases from 516.7 K to 531.1 K (Fig. S7). However, η_{chem} only improves from 29.02 % to the peak value of 29.06 % (blue dashed line in Fig. 4a). Further reducing the flow rate to increase T_{sem} intensifies radiative recombination (Fig. 4b), resulting in a significant negative impact on $\eta_{quantum}$. This adverse effect outweighs the positive influence of bandgap reduction on η_{chem}, leading to a decline in η_{chem}. Nevertheless, η_{total} continues to rise after η_{chem} begins to decrease due to $\eta_{thermal}$ is still enhanced by the increasing T_{sem} (Fig. 4a). Therefore, the η_{total} ultimately reaches a peak of 35.54 % when the flow rate reduces to 0.35 kg/s (yellow dashed line in Fig. 4a).

4.2. Regulating T_{gap} by reducing H

Although reducing the flow rate can improve both η_{chem} and $\eta_{thermal}$ by elevating T_{sem}, its effects on narrowing the T_{gap} is limited. T_{gap} remains above 100 K even the flow rate decreases to 0.35 kg/s (Fig. S7), which indicates that the potential of T_{sem} to improve $\eta_{thermal}$ has been fully exploited. The reason reducing the flow rate fails to effectively narrow T_{gap} is that it does not significantly enhance convective heat transfer (Fig. S8). Therefore, we try to reduce the hydraulic diameter (d_e) of the flow channel by decreasing H (Equation (S28)) to enhance convective heat transfer. [47,48] The results indicates that reducing H effectively increases the convective heat transfer coefficient (Fig. S9), thereby significantly reducing T_{gap}. When H is reduced to 100 μm, T_{gap} falls below 10 K even at C = 1000 (Fig. S10), fully unleashing the capacity of T_{sem} to generate thermal exergy. However, enhancing convective heat transfer leads to a reduction in T_{sem} (Fig. S10), which decreases both η_{chem} and η_{total} (Fig. S11).

4.3. Regulating T_{sem} and T_{gap} with combined approach

These results indicate that reducing H and reducing flow rate should be combined to simultaneously increase T_{sem} and narrow T_{gap}. We reduce H to 100 μm, while the flow rate is decreaseed from 1 kg/s to 0.1 kg/s. For comparison with the case in Fig. 4a, where only the flow rate is reduced, T_{sem} rather than the flow rate is used as the independent variable in Fig. 4c. The overlap of η_{chem} in the two cases demonstrates that η_{chem} is exclusively determined by T_{sem} (Fig. 4c), regardless of the heat transfer adjustments employed to achieve T_{sem} (Fig. S12). This is becausethe photon incident rate is constant under a fixed C, while the photon absorption rate and recombination rate depend solely on T_{sem} (Equations (S1) and (S10)). Consequently, both $\eta_{quantum}$ and η_{chem} are determined by T_{sem}. However, under the same T_{sem}, $\eta_{thermal}$ is higher when using the combined approach compared to reducing the flow rate

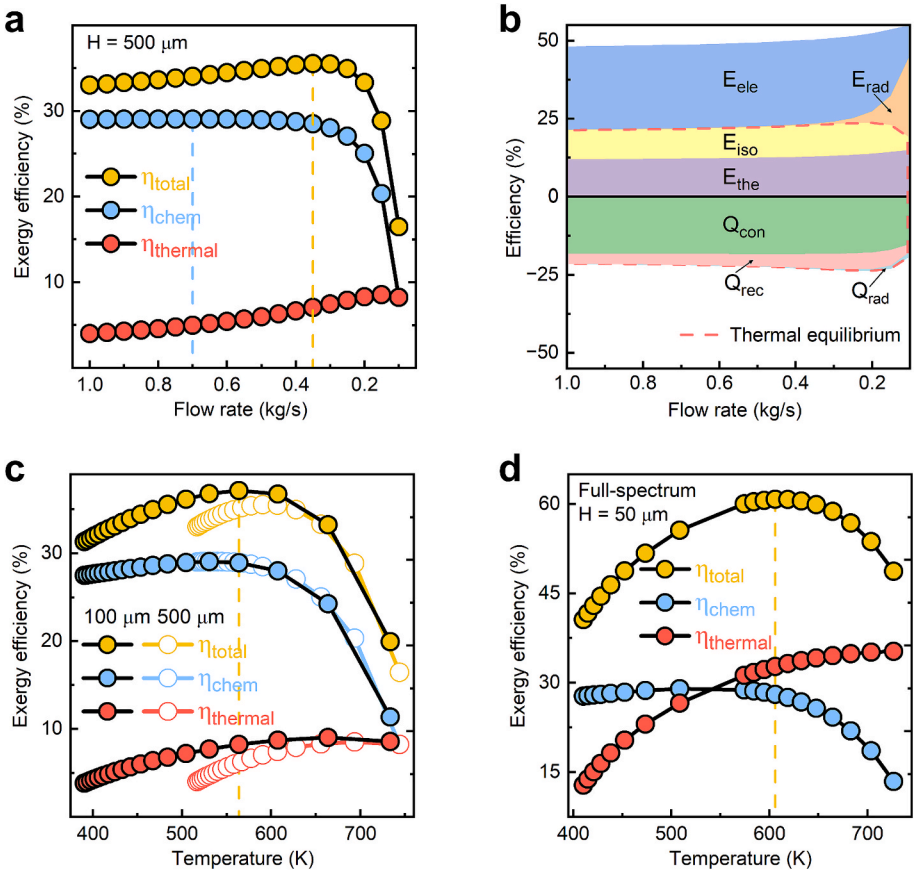

Fig. 4. Optimizing η_{total} by regulating temperature effects through heat transfer adjustments. (a) Variations in η_{chem}, $\eta_{thermal}$ and η_{total} with reducing flow rate when H is 500 μm. (b) Variations in energy conservation and TE with reducing flow rate when H is 500 μm. (c) Variations in η_{chem}, $\eta_{thermal}$ and η_{total} with reducing flow rate when H is 500 μm and 100 μm, respectively. T_{sem} instead of the flow rate is set as the independent variable for comparison, and the flow rate is still reduced from 1 kg/s to 0.1 kg/s. (d) Variations in η_{chem}, $\eta_{thermal}$ and η_{total} in the full-spectrum utilization mode. H is 50 μm, and the flow rate is reduced from 5 kg/s to 0.5 kg/s. T_{sem} instead of the flow rate is set as the independent variable. In (a)-(d), the E_{g0} of semiconductor catalysts and C are 1.8 eV and 1000, respectively. The blue and yellow dash lines indicate the peak value of η_{chem} and η_{total}, respectively.

alone, as the reduction in H results in a smaller T_{gap} (Fig. S13). The enhancement of $\eta_{thermal}$ increases the peak η_{total} from 35.54 % in Fig. 4a to 37.16 %, where T_{sem} = 563.8 K and the flow rate is 0.25 kg/s (Fig. 4c). This peak value represents the optimal η_{total} for this ideal PTC system when C = 1000 and E_{g0} = 1.8 eV, as the potential of $\eta_{thermal}$ is also fully exploited (T_{gap} approaches zero).

5. Full-spectrum utilization and broad-range calculations

5.1. Full-spectrum utilization

The contribution of $\eta_{thermal}$ to η_{total} is relatively small. It accounts for only 22.2 % even at the optimal η_{total}, (Fig. 4c). This is primarily due to the necessity of a sufficiently large bandgap to drive the reaction, which limits the light absorption. For instance, 48.7 % of the incident light (AM 1.5G) remains unabsorbed with a bandgap of 1.8 eV. In contrast, photovoltaics are not constrained by this limitation. Silicon cells, with a bandgap of 1.1 eV, are capable of absorbing up to 80 % of incident light. This comparison underscores the critical importance of full-spectrum utilization for PTC systems.

The potential for full-spectrum utilization in the ideal PTC system was explored using this model. It is assumed that the light not absorbed by the catalyst plate will pass through entirely and be absorbed by the heat collection membrane integrated beneath the catalyst plate, where it is fully converted into thermal energy. The membrane is assumed to be at the same temperature as the catalyst plate due to its thin structure and close adherence. The combined approach for optimizing η_{total} remains applicable to the full-spectrum PTC system. The required flow rate for achieving the same T_{sem} is higher due to the increased Q_{source} introduced by the heat collection membrane.

The increased flow rate requires a smaller H to enhance convective heat transfer and maintain a sufficiently low T_{gap}. We found that an H of 50 μm ensures that T_{gap} remains below 10 K (Fig. S14). η_{chem} of the full-spectrum PTC system remains solely dependent on T_{sem} (Fig. S15). However, $\eta_{thermal}$ improves significantly due to the increased Q_{source}. For instance, $\eta_{thermal}$ increases to ~29 % at T_{sem} = 550 K (Fig. 4d), which is only ~8 % under standard mode at the same T_{sem} (Fig. 4c). The increase of $\eta_{thermal}$ substantially enhances η_{total}. The peak value of η_{total} reaches 60.79 % at T_{sem} = 606.1 K when the flow rate is 0.85 kg/s (yellow dash line in Fig. 4d), and the contribution rate of $\eta_{thermal}$ reaches 53.8 %.

5.2. Broad-range calculations

We explored the theoretical exergy efficiencies of PTC systems in a broad range. The range of E_{g0} and C is 1.5 eV to 3.5 eV, and 100 to 1000, respectively. A uniform heat transfer condition for all values of E_{g0} and C for comparison, which is the heat transfer condition for optimal η_{total} when C = 1000 and E_{g0} = 1.8 eV. For standard PTC systems, the heat transfer condition is a flow rate of 0.25 kg/s and H = 100 μm (Fig. 4c). When E_{g0} is below 1.8 eV, η_{chem} decreases with increasing C and may even approach zero (Fig. 5a). This is because the rise in T_{sem} leads to excessive radiative recombination, significantly diminishing $\eta_{quantum}$. When E_{g0} exceeds 1.75 eV, η_{chem} consistently increases up to C = 1000. This is because radiative recombination becomes more tolerant to increasing T_{sem} for larger E_{g0} (Fig. S16), allowing $\eta_{quantum}$ to persistently benefit from the reduction of bandgap with higher T_{sem}. $\eta_{thermal}$ increases with higher C and lower E_{g0} (Fig. 5b) due to the elevated T_{sem} (Fig. S17). The small value of H ensures that T_{gap} remains below 0.3 K (Fig. S17), allowing the full potential of $\eta_{thermal}$ to be realized. The combination of η_{chem} and $\eta_{thermal}$ results in excellent performance of η_{total} (Fig. 5c). The

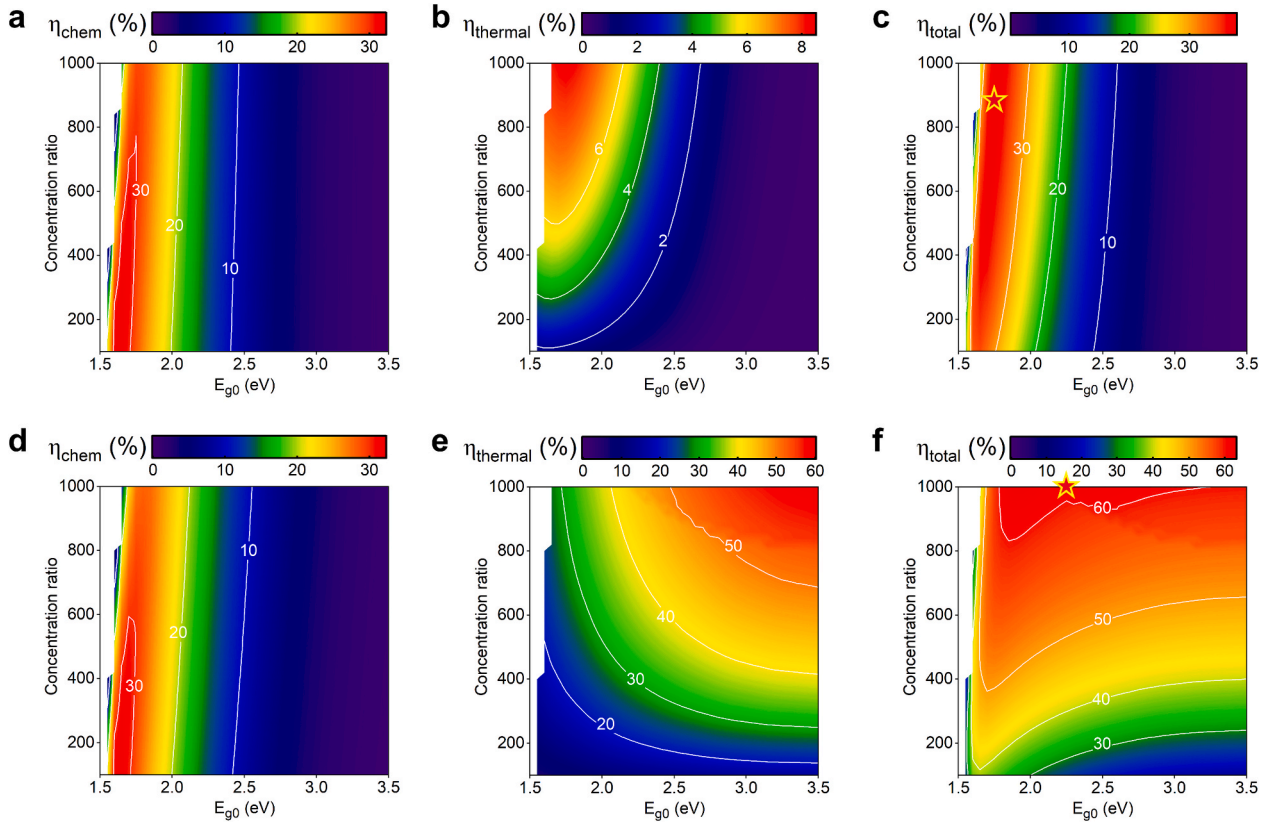

Fig. 5. Calculations over a wide range of E_{g0} and C. (a) η_{chem}, (b) $\eta_{thermal}$, and (c) η_{total} of the standard PTC system with a flow rate of 0.25 kg/s and H = 100 μ m. The pentagram in (c) indicates the optimal η_{total} in standard mode. The value is 37.64 %, corresponding E_{g0} and C are 1.75 eV and 880, respectively. (d) η_{chem}, (c) $\eta_{thermal}$, and (f) η_{totall} of the PTC system in the full-spectrum utilization mode with a flow rate of 0.85 kg/s and H = 50 μ m. The pentagram in (f) indicates the optimal η_{total} in full-spectrum mode. The value is 62.87 %, corresponding E_{g0} and C are 2.25 eV and 1000, respectively.

maximum η_{total} reaches 37.64 % at E_{g0} = 1.75 eV and C = 880, with a η_{chem} of 29.73 %.

For full-spectrum PTC systems, the heat transfer condition is a flow rate of 0.85 kg/s and H = 50 μm (Fig. 4d). η_{chem} and $\eta_{thermal}$ exhibit a complementary relationship under full-spectrum mode. η_{chem} dominates at smaller E_{g0} values (Fig. 5d), while $\eta_{thermal}$ becomes the primary contributor at larger E_{g0} values (Fig. 5e), as the increase in unabsorbed light with larger E_{g0} significantly raises the Q_{source} and T_{sem} (Fig. S18). This complementary relationship ensures a high η_{total} across the entire range of C and E_{g0} (Fig. 5f). η_{total} consistently exceeds 40 % when C > 400 and surpasses 50 % when C > 600. The maximum η_{total} reaches 62.87 % at E_{g0} = 2.25 eV and C = 1000.

6. Limitations and future research

6.1. Limitations and future research of the model

This model focuses on establishing CB–TE coupling to predict η_{chem}, $\eta_{thermal}$, and η_{total} in high-temperature PTC systems, and therefore adopts several simplifications in other aspects. The limitations associated with these simplifications, as well as potential pathways for future improvements, are discussed below:

(1) Non-radiative recombination. In practical materials, non-radiative recombination must be considered. It not only affects CB but also acts as a thermal source participating in TE through CB–TE coupling [38].
(2) Tandem semiconductors. If tandem semiconductors are used to further enhance η_{total}, the coupling of CB between different semiconductor layers needs to be established [30].
(3) TE. The current TE does not account for internal thermal conduction within the material. For materials with significant thickness, thermal conduction must be incorporated. In cases involving tandem semiconductors or integrated selective absorbing heat-collecting films, interfacial heat transfer between layers also should be explicitly modeled.
(4) Chemical reactions. The model does not consider phase transitions or reaction kinetics of chemical reactions, both of which are essential for realistic PTC systems.

For limitation (1), we have reserved an interface to accommodate non-radiative recombination (see E_{nonrad} in Equations (8) and (9)), allowing non-radiative recombination characteristics of real materials to be incorporated. To address limitations (2), (3), and (4), the relevant governing equations can be integrated into the current model framework. Another efficient solution is to incorporate this model as the CB–TE coupling module into commercial multiphysics platforms such as Fluent or COMSOL, leveraging their mature capabilities in heat transfer, multiphase flow, and reaction kinetics. This is also the direction of our future work.

6.2. Practical applications of high-temperature PTC systems

Significant progress has been made in the practical application of high-temperature PTC systems at the material, device, and system levels. However, many critical challenges remain to be addressed:

(1) Materials. Semiconductors such as AlGaInP and GaInP have demonstrated power conversion efficiencies exceeding 10 % in photovoltaic at temperatures above 600 K, with bandgaps around 2 eV [48,49]. These materials can be fabricated via chemical vapor deposition (CVD), which is compatible with existing industrial infrastructure. However, severe non-radiative recombination at elevated temperatures remains a major limitation. Further advances in defect passivation, interface engineering, and structural optimization are required to suppress recombination and extend device longevity.
(2) Devices. The microchannel dimensions used for cooling in this model (50–500 μm) are common in current industrial applications [50] However, the associated manufacturing costs still require further reduction. The use of tandem semiconductors is expected to further enhance η_{total} of PTC systems, and some progress has already been reported on tandem devices operating at high temperatures [48] Nevertheless, achieving high interfacial carrier transport efficiency, efficient thermal conduction between layers, and mechanical compatibility under thermal stress remains a challenge. These issues depend heavily on future advancements in materials and device architecture. Furthermore, realizing full-spectrum utilization will require the integration of semiconductor films with selective-absorbing heat-collecting films.
(3) Systems. The cost of optical concentrator components is steadily decreasing with the rapid advancement of concentrated solar power technologies [43]. System-level modeling and optimization require further advancement, particularly in the coordinated management of multiple energy flows—including optical, thermal, and chemical energy.

7. Conclusion

In this work, we develop a theoretical model for high-temperature PTC systems by establishing CB-TE coupling and apply it to an idealized PTC system. Our analysis demonstrates that the complex influence of thermal effects on non-thermal effects—including chemical reactions and semiconductor performance—can be effectively captured by a single parameter: $\eta_{quantum}$. By modulating T_{sem} to enhance $\eta_{quantum}$, thermal and non-thermal effects can be synergistically coordinated, resulting in η_{chem} to exceed 32 % (No. 8 in Table 1), which surpasses the predictions of previous low-temperature theoretical models. Furthermore, we propose a generalized strategy for manipulating thermal effects based on two characteristic temperatures—T_{sem} and T_{gap}. This strategy enables the joint optimization of η_{chem} and $\eta_{thermal}$, thereby maximizing η_{total} of PTC systems. In addition, we demonstrate that η_{total} can be further enhanced through full-spectrum utilization by converting sub-bandgap radiation into thermal energy. Extensive calculations indicate that the theoretical η_{total} can exceed 37 % under standard mode and surpass 60 % under full-spectrum utilization, significantly outperforming the Shockley–Queisser limit of single-junction semiconductors. Finally, we discuss the current limitations and future directions for both the theoretical modeling and practical deployment of high-temperature PTC systems. In summary, this work deepens the fundamental understanding of high-temperature PTC systems and establishes a robust framework for predicting performance and guiding optimization, providing critical insights for advancing high-temperature PTC technologies toward highly efficient and sustainable energy solutions.

CRediT authorship contribution statement

Yuan Gao: Writing – review & editing, Writing – original draft, Visualization, Validation, Software, Methodology, Formal analysis, Data curation, Conceptualization. **Chenyu Xu:** Writing – review & editing, Supervision, Project administration, Funding acquisition. **Entao Zhang:** Validation, Software, Conceptualization. **Xuan Zhu:** Writing – review & editing, Visualization, Methodology, Conceptualization. **Yin Xie:** Writing – review & editing, Visualization, Methodology. **Yanwei Zhang:** Writing – review & editing, Supervision, Project administration, Funding acquisition, Conceptualization.

Declaration of competing interest

The authors declare that they have no known competing financial interests or personal relationships that could have appeared to influence the work reported in this paper.

Acknowledgments

This work is supported by the National Natural Science Foundation of China (52341602), Zhejiang Provincial Natural Science Foundation of China under Grant No. LDT23E06014E06, Zhejiang Provincial Natural Science Foundation of China under Grant No. LQ24E060001, National Key Research and Development Project (2023YFC3710800), and the Fundamental Research Funds for the Central Universities (2022ZFJH04).

Appendix A. Supplementary data

Supplementary data to this article can be found online at https://doi.org/10.1016/j.enconman.2025.120062.

Data availability

Data will be made available on request.

References

[1] Kannan N, Vakeesan D. Solar energy for future world: a review. Renew Sust Energ Rev 2016;62:1092–105. https://doi.org/10.1016/j.rser.2016.05.022.
[2] Peters IM, Buonassisi T. Energy yield limits for single-junction solar cells. Joule 2018;2:1160–70. https://doi.org/10.1016/j.joule.2018.03.009.
[3] He Y, Hamann T, Wang D. Thin film photoelectrodes for solar water splitting. Chem Soc Rev 2019;48:2182–215. https://doi.org/10.1039/c8cs00868j.
[4] Kim JH, Hansora D, Sharma P, Jang JW, Lee JS. Toward practical solar hydrogen production - an artificial photosynthetic leaf-to-farm challenge. Chem Soc Rev 2019;48:1908–71. https://doi.org/10.1039/c8cs00699g.
[5] Anand B, Shankar R, Murugavelh S, Rivera W, Midhun Prasad K, Nagarajan R. A review on solar photovoltaic thermal integrated desalination technologies. Renew Sust Energ Rev 2021;141:110787. https://doi.org/10.1016/j.rser.2021.110787.
[6] Farrell DJ, Sodabanlu H, Wang Y, Sugiyama M, Okada Y. A hot-electron thermophotonic solar cell demonstrated by thermal up-conversion of sub-bandgap photons. Nat Commun 2015;6:8685. https://doi.org/10.1038/ncomms9685.
[7] Aydin E, Allen TG, De Bastiani M, Xu L, Ávila J, Salvador M, et al. Interplay between temperature and bandgap energies on the outdoor performance of perovskite/silicon tandem solar cells. Nat Energy 2020;5:851–9. https://doi.org/10.1038/s41560-020-00687-4.
[8] Krogstrup P, Jørgensen HI, Heiss M, Demichel O, Holm JV, Aagesen M, et al. Single-nanowire solar cells beyond the Shockley–Queisser limit. Nat Photonics 2013;7:306–10. https://doi.org/10.1038/nphoton.2013.32.
[9] Wan L, Zhou Q, Wang X, Wood TE, Wang L, Duchesne PN, et al. Cu_2O nanocubes with mixed oxidation-state facets for (photo)catalytic hydrogenation of carbon dioxide. Nat Catal 2019;2:889–98. https://doi.org/10.1038/s41929-019-0338-z.
[10] Hisatomi T, Domen K. Reaction systems for solar hydrogen production via water splitting with particulate semiconductor photocatalysts. Nat Catal 2019;2:387–99. https://doi.org/10.1038/s41929-019-0242-6.
[11] Park S, Chang WJ, Lee CW, Park S, Ahn H-Y, Nam KT. Photocatalytic hydrogen generation from hydriodic acid using methylammonium lead iodide in dynamic equilibrium with aqueous solution. Nat Energy 2016;2:16185. https://doi.org/10.1038/nenergy.2016.185.
[12] Guillemoles J-F, Kirchartz T, Cahen D, Rau U. Guide for the perplexed to the Shockley–Queisser model for solar cells. Nat Photonics 2019;13:501–5. https://doi.org/10.1038/s41566-019-0479-2.
[13] Daneshazarian R, Cuce E, Cuce PM, Sher F. Concentrating photovoltaic thermal (CPVT) collectors and systems: Theory, performance assessment and applications. Renew Sust Energ Rev 2018;81:473–92. https://doi.org/10.1016/j.rser.2017.08.013.
[14] Zhou P, Navid IA, Ma Y, Xiao Y, Wang P, Ye Z, et al. Solar-to-hydrogen efficiency of more than 9% in photocatalytic water splitting. Nature 2023;613:66–70. https://doi.org/10.1038/s41586-022-05399-1.
[15] Hong J, Xu C, Deng B, Gao Y, Zhu X, Zhang X, et al. Photothermal chemistry based on solar energy: from synergistic effects to practical applications. Adv Sci 2021;9:2103926. https://doi.org/10.1002/advs.202103926.
[16] Wang K, Ren Y, Wang N, Cheng M, Zhou J, Ge Y, et al. Band-division utilization of core-shell photocatalyst under condenser solar-light and enhancement of synergistic catalytic CO_2 reduction. Chem Eng J 2024;479:147529. https://doi.org/10.1016/j.cej.2023.147529.
[17] Xu L, Ren Y, Fu Y, Liu M, Zhu F, Cheng M, et al. Strong photo-thermal coupling effect boosts CO_2 reduction into CH4 in a concentrated solar reactor. Chem Eng J 2023;468:143831. https://doi.org/10.1016/j.cej.2023.143831.
[18] Wu M, Ren Y, Zhu F, Zhou J, Ma Q, Huang K, et al. Photothermal coupling effect boosts the conversion of CO_2 to solar fuel over Pt/ZnO photocatalyst in a concentrated solar reactor. Ind Eng Chem Res 2023;62:9463–73. https://doi.org/10.1021/acs.iecr.3c01279.
[19] Singh P, Ravindra NM. Temperature dependence of solar cell performance—an analysis. Sol Energy Mater Sol Cells 2012;101:36–45. https://doi.org/10.1016/j.solmat.2012.02.019.
[20] Meneses-Rodríguez D, Horley PP, González-Hernández J, Vorobiev YV, Gorley PN. Photovoltaic solar cells performance at elevated temperatures. Sol Energy 2005;78:243–50. https://doi.org/10.1016/j.solener.2004.05.016.
[21] Ju X, Xu C, Han X, Du XZ, Wei GS, Yang YP. A review of the concentrated photovoltaic/thermal (CPVT) hybrid solar systems based on the spectral beam splitting technology. Appl Energy 2017;187:534–63. https://doi.org/10.1016/j.apenergy.2016.11.087.
[22] Yuan W, Ji J, Modjinou M, Zhou F, Li Z, Song Z, et al. Numerical simulation and experimental validation of the solar photovoltaic/thermal system with phase change material. Appl Energy 2018;232:715–27. https://doi.org/10.1016/j.apenergy.2018.09.096.
[23] Herez A, El Hage H, Lemenand T, Ramadan M, Khaled M. Review on photovoltaic/thermal hybrid solar collectors: classifications, applications and new systems. Sol Energy 2020;207:1321–47. https://doi.org/10.1016/j.solener.2020.07.062.
[24] Zhang X, Xu C, Zhang L, Li Z, Hong J, Zhang Y. Photothermal catalytic water splitting at diverse two-phase interfaces based on Cu–TiO_2. ACS Appl Energy Mater 2022;5:4564–76. https://doi.org/10.1021/acsaem.2c00009.
[25] Xie Y, Xu C, Liu Y, Zhang E, Chen Z, Zhan X, et al. Photothermal synergistic hydrogen production via a fly-ash-made interfacial Vaporific system. Adv Sci 2025;12:e2410201. https://doi.org/10.1002/advs.202410201.
[26] Xu M, Hu X, Wang S, Yu J, Zhu D, Wang J. Photothermal effect promoting CO_2 conversion over composite photocatalyst with high graphene content. J Catal 2019;377:652–61. https://doi.org/10.1016/j.jcat.2019.08.010.
[27] Holmes-Gentle I, Tembhurne S, Suter C, Haussener S. Kilowatt-scale solar hydrogen production system using a concentrated integrated photoelectrochemical device. Nat Energy 2023;8:586–96. https://doi.org/10.1038/s41560-023-01247-2.
[28] Tembhurne S, Nandjou F, Haussener S. A thermally synergistic photo-electrochemical hydrogen generator operating under concentrated solar irradiation. Nat Energy 2019;4:399–407. https://doi.org/10.1038/s41560-019-0373-7.
[29] Bolton JR, Strickler SJ, Connolly JS. Limiting and realizable efficiencies of solar photolysis of water. Nature 1985;316:495–500. https://doi.org/10.1038/316495a0.
[30] Rocheleau RE, Miller EL. Photoelectrochemical production of hydrogen: engineering loss analysis. Int J Hydrogen Energy 1997;22:771–82. https://doi.org/10.1016/S0360-3199(96)00221-2.
[31] Hu S, Xiang C, Haussener S, Berger AD, Lewis NS. An analysis of the optimal band gaps of light absorbers in integrated tandem photoelectrochemical water-splitting systems. Energ Environ Sci 2013;6:2984–93. https://doi.org/10.1039/c3ee40453f.
[32] Haussener S, Hu S, Xiang C, Weber AZ, Lewis NS. Simulations of the irradiation and temperature dependence of the efficiency of tandem photoelectrochemical water-splitting systems. Energ Environ Sci 2013;6:3605. https://doi.org/10.1039/c3ee41302k.
[33] Chen Y, Xiang C, Hu S, Lewis NS. Modeling the Performance of an integrated photoelectrolysis system with 10 × solar concentrators. J Electrochem Soc 2014;161:F1101–10. https://doi.org/10.1149/2.0751410jes.
[34] Ye X, Melas-Kyriazi J, Feng ZA, Melosh NA, Chueh WC. A semiconductor/mixed ion and electron conductor heterojunction for elevated-temperature water splitting. PCCP 2013;15:15459–69. https://doi.org/10.1039/c3cp52536h.
[35] Huang, K. (1988). Solid state physics (Higher Education Press).
[36] Yu B, Jiang Q, He W, Liu S, Zhou F, Ji J, et al. Performance study on a novel hybrid solar gradient utilization system for combined photocatalytic oxidation technology and photovoltaic/thermal technology. Appl Energy 2018;215:699–716. https://doi.org/10.1016/j.apenergy.2018.02.017.
[37] Xu L, Liu W, Liu H, Ke C, Wang M, Zhang C, et al. Heat generation and mitigation in silicon solar cells and modules. Joule 2021;5:631–45. https://doi.org/10.1016/j.joule.2021.01.012.
[38] Hajjiah A. COMSOL simulation of non-radiative recombination heat and joule heat in CZTSSe thin film solar cells. Micro Nano Struct 2022;168:207313. https://doi.org/10.1016/j.micrna.2022.207313.
[39] Han J, Lu L, Yang H. Numerical evaluation of the mixed convective heat transfer in a double-pane window integrated with see-through a-Si PV cells with low-e coatings. Appl Energy 2010;87:3431–7. https://doi.org/10.1016/j.apenergy.2010.05.025.
[40] Shockley W, Queisser HJ. Detailed balance limit of efficiency of p-n junction solar cells. J Appl Phys 1961;32:510–9. https://doi.org/10.1063/1.1736034.
[41] Zheng D, Yue X, Wang Z, Fan S, Zhang Z, Dai W, et al. Investigation into the photothermal catalytic CO2 decomposition over CeO2 with different morphologies: behaviors of oxygen vacancies. Sep Purif Technol 2024;350:127973. https://doi.org/10.1016/j.seppur.2024.127973.
[42] Yang, S., and Tao, W. (2006). Heat transfer (Higher Education Press).
[43] Valenzuela L, López-Martín R, Zarza E. Optical and thermal performance of large-size parabolic-trough solar collectors from outdoor experiments: a test method and a case study. Energy 2014;70:456–64. https://doi.org/10.1016/j.energy.2014.04.016.

[44] Passler R. Basic model relations for temperature dependencies of fundamental energy gaps in semiconductors. Phys Status Solidi B Basic Solid State Phys 1997; 200:155–72. https://doi.org/10.1002/1521-3951(199703)200:1<155::Aid-pssb155>3.0.Co;2-3.
[45] Passler R. Parameter sets due to fittings of the temperature dependencies of fundamental bandgaps in semiconductors. Phys Status Solidi B Basic Solid State Phys 1999;216:975. https://doi.org/10.1002/%28SICI%291521-3951%28199912%29216%3A2<975%3A%3AAID-PSSB975>3.0.CO%3B2-N.
[46] Giteau M, de Moustier E, Suchet D, Esmaielpour H, Sodabanlu H, Watanabe K, et al. Identification of surface and volume hot-carrier thermalization mechanisms in ultrathin GaAs layers. J Appl Phys 2020;128:193102. https://doi.org/10.1063/5.0027687.
[47] Tiwari GN, Mishra RK, Solanki SC. Photovoltaic modules and their applications: a review on thermal modelling. Appl Energy 2011;88:2287–304. https://doi.org/10.1016/j.apenergy.2011.01.005.
[48] Perl EE, Simon J, Geisz JF, Olavarria W, Young M, Duda A, et al. Development of high-bandgap AlGaInP solar cells grown by organometallic vapor-phase epitaxy. IEEE J Photovolt 2016;6:770–6. https://doi.org/10.1109/jphotov.2016.2537543.
[49] Perl EE, Kuciauskas D, Simon J, Friedman DJ, Steiner MA. Identification of the limiting factors for high-temperature GaAs, GaInP, and AlGaInP solar cells from device and carrier lifetime analysis. J Appl Phys 2017;122:233102. https://doi.org/10.1063/1.5003631.
[50] Lee P-S, Garimella SV, Liu D. Investigation of heat transfer in rectangular microchannels. Int J Heat Mass Transf 2005;48:1688–704. https://doi.org/10.1016/j.ijheatmasstransfer.2004.11.019.